# Evolution of carbon nanostructure during pyrolysis of homogeneous chitosan-cellulose composite fibers

Hilda Zahra, Daisuke Sawada, Shogo Kumagai, Yu Ogawa, Leena-Sisko Johansson, Yanling Ge, Chamseddine Guizani, Toshiaki Yoshioka, Michael Hummel

Carbon 185 (2021) 27–38

Contents lists available at ScienceDirect

Carbon

journal homepage: www.elsevier.com/locate/carbon

Research Paper

# Evolution of carbon nanostructure during pyrolysis of homogeneous chitosan-cellulose composite fibers

Hilda Zahra [a], Daisuke Sawada [a], Shogo Kumagai [b], Yu Ogawa [c], Leena-Sisko Johansson [a], Yanling Ge [d, 1], Chamseddine Guizani [a], Toshiaki Yoshioka [b], Michael Hummel [a, *]

[a] Department of Bioproducts and Biosystems, Aalto University, Vuorimiehentie 1, 02150, Espoo, Finland
[b] Graduate School of Environmental Studies, Tohoku University, 6-6-07 Aoba, Aramaki-aza, Aoba-ku, 980-8579, Sendai, Japan
[c] Univ. Grenoble Alpes, CNRS, CERMAV, 38000, Grenoble, France
[d] Department of Chemistry and Material Sciences, Aalto University, Kemistintie 1, 02150, Espoo, Finland

ARTICLE INFO

*Article history:*
Received 21 May 2021
Received in revised form
20 August 2021
Accepted 21 August 2021
Available online 7 September 2021

*Keywords:*
Cellulose
Chitosan
Carbon fiber
Dehydration catalyst
Pyrolysis
Carbon nanostructure

ABSTRACT

Chitosan-cellulose composite fibers spun using a Lyocell technology are characterized by a homogeneous distribution and a close packing of the two biopolymers inside the fibrous matrix. Due to the intimate contact of cellulose and chitosan, synergistic effects can be observed during the pyrolysis of the composite fibers. In this study, the catalytic role of chitosan in altering the cellulose pyrolysis pathway in the composite fibers at moderate treatment temperatures up to 900 °C is confirmed. Analyses of the evolved gases during pyrolysis revealed that chitosan promoted cellulose dehydration and substantially decreased the formation of levoglucosan, explaining the higher char yield. The enhanced dehydration reaction is associated with the formation of intermolecular crosslinks due to the incorporation of nitrogen from chitosan in the resulting carbon structures. Nitrogen could also contribute to the in-plane disorder in the aromatic clusters when the pyrolysis is carried out at 500–700 °C, although the in-plane disorder is less noticeable from 700 to 900 °C. Nevertheless, the size of the aromatic cluster continues to grow when the composite fibers are pyrolyzed in a temperature range of 500–900 °C.


## 1. Introduction

Due to its abundance on earth, cost-effectiveness, non-toxicity, and excellent mechanical strength and flexibility, cellulose plays an important role as a source of renewable materials and energy [1,2]. Cellulose-based carbon materials can be produced through various thermochemical routes, such as pyrolysis, and show potential in various applications such as for environmental remediation (pollutant and heavy metal adsorption) [1], energy storage (electrode material in batteries and supercapacitors) [2–9], structural applications (carbon fibers and composite materials) [10], and catalysis [11,12].

In the course of cellulose pyrolysis, the product distributions are mostly governed by two competing pathways. The first pathway described by Shafizadeh favors the formation of gaseous and solid products, while the second one favors the formation of condensable liquid products or tars [13]. The reactions involved in the first pathway are dominant at low temperature (≤300 °C) and include reduction in molecular weight or degree of polymerization (DP) by bond scission, dehydration, rearrangement, production of carbon dioxide and carbon monoxide, and char formation [13–16]. The rate-limiting step in the first pathway is the dehydration reaction, which can be accelerated by incorporating dehydration catalysts [15–17]. When the pyrolysis temperature is high enough to overcome the activation energy of depolymerization (~200 kJ/mol) [18], usually around 300–500 °C [13], the second pathway or depolymerization of the cellulose chains is favored, producing tars, wherein levoglucosan is the major product (up to 80%) [19]. The dominance of depolymerization over dehydration lowers the char yield (~10 wt%) compared to its theoretical maximum yield (44.4 wt%) [20]. Therefore, for pyrolysis at high temperatures or heating rates, the presence of catalysts is required to promote the first pathway and consequently to improve the char yield [16]. An increased carbon yield improves the economic feasibility and process sustainability in the production of carbonaceous materials from cellulose.

* Corresponding author.
*E-mail address:* michael.hummel@aalto.fi (M. Hummel).
[1] Current address: VTT Technical Research Center of Finland Ltd.

https://doi.org/10.1016/j.carbon.2021.08.062

In our recent study [21], chitosan, an amine-containing cellulose analog, substantially increased the yield of carbon fibers derived from cellulose composite fibers prepared via a recently developed Lyocell-type spinning process termed Ioncell®. In this process, cellulose and chitosan are dissolved simultaneously in a non-derivatizing solvent and the solution is spun into an aqueous coagulation bath. The resulting fiber matrix consists of highly oriented cellulose polymer chains in which chitosan is homogeneously distributed. The intimate contact between cellulose and the amine groups presents in chitosan altered the cellulose degradation during pyrolysis observed via differential thermogravimetry (DTG). The comparison with DTG results of the simple physical mixture of cellulose and chitosan powder showed that the composite fiber had a significantly lower rate of cellulose degradation compared to the physical mixture.

Inorganic salts, such as $(NH_4)_2SO_4$, $(NH_4)_2HPO_4$, and $NH_4Cl$, are commonly used as dehydration catalysts to enhance the flame retardancy and the char yield of cellulosic materials. For this purpose, the catalysts are required to exhibit several characteristics: (i) decrease the pyrolysis temperature, (ii) increase the release of water and carbon dioxide, and (iii) increase the amount of char formed [14,15,22].

Therefore, to elucidate the catalytic effect of chitosan during the pyrolysis of the composite fibers, we investigated the formation of water and $CO_2$ and their onset temperatures via evolved gas analysis-mass spectrometry. In addition, we also monitored the production of levoglucosan as the main compound from tar. The results from the composite fibers are also compared to the physical mixture of cellulose and chitosan powder similar to our previous study [21]. Furthermore, we carried out an in-depth nano-structure characterization of the pyrolytic carbon material. These are important aspects for the development of not only cellulose-based carbon fibers but also novel heteroatom-doped carbon materials, particularly nitrogen-doped carbon, which offer potential applications in various fields [23,24]. To the best of our knowledge, this study is the first one examining the role of chitosan as a dehydration catalyst during cellulose pyrolysis with an additional focus on the effect of nitrogen on the carbon nanostructure evolving at moderate pyrolysis temperatures (up to 900 °C). The structure formation at such comparatively low temperatures is not fully understood yet but is of high interest both in terms of economic and ecological impact of biomass pyrolysis.

## 2. Materials and methods

### 2.1. Preparation of chitosan-cellulose composite fibers

Birch (*Betula pendula*) prehydrolysis kraft pulp (PHK) ([η] = 494 ml/g, Mn = 72.9 kDa, Mw = 262.9 kDa, polydispersity 3.6, Enocell Speciality Cellulose, Finland) was received from Stora Enso Enocell Mill in Finland. The cellulose was received as pulp sheets and ground to a fine powder in a Wiley mill before use. Chitosan powder was purchased from Glentham Life Scince (UK), having average molecular weights of 30 kDa.

In brief, the chitosan was dissolved in ionic liquid (IL) 1,5-diazabicyclo[4.3.0]non-5-ene-1-ium acetate ([DBNH]OAc). Then, the cellulose pulp was added to the chitosan-IL solution and continuously mixed until both polymers were completely dissolved. The chitosan/cellulose polymer shares were 10/90 or 25/75 (w/w) and the total polymer concentration in the IL solution was 12 wt%. A reference solution of 100% cellulose was also prepared. Due to the significantly lower molecular weight of chitosan, it was not possible to spin a 100% chitosan fiber using the IL-based dry-jet wet spinning technology. The viscoelastic properties of a pure chitosan solution did not allow for filament stretching in the air gap but instead showed instant filament breach. Further, chitosan is substantially more expensive than pulp cellulose. Therefore, composite fibers with higher chitosan shares were not prepared.

The chitosan-cellulose composite fibers were spun in a customized dry jet-wet spinning unit (Fourné Polymertechnik, Germany). The take-up velocity and extrusion velocity were adjusted so that the spun fibers had a draw ratio (DR) of 4. The collected continuous filament was washed and air-dried. The details for the preparation of the spinning solutions and the spinning of the chitosan-cellulose composite fibers can be found elsewhere [21].

### 2.2. Preparation of carbon fibers derived from chitosan-cellulose composite fibers

Carbon fibers were prepared by carbonizing ~300 mg of the oven-dried precursor fibers (~10 cm length) in a tubular furnace (NBD Tube Furnace). The samples were placed in a ceramic boat, heated under a flow of $N_2$ of 8.3 l/min from room temperature to the final temperature (500, 700, or 900 °C) using a heating rate of 10 °C/min. The carbonization was held for 30 min at the final temperature before cooling down to room temperature [21].

### 2.3. Characterization of composite fibers and carbon fibers

#### 2.3.1. Characterization of pyrolysis products from composite fibers

Evolved gas analysis-mass spectrometry (EGA-MS) experiments were carried out to semi-quantify the formation of water, $CO_2$, and levoglucosan during pyrolysis. A Multi-shot pyrolyzer (EGA/Py-3030D, Frontier Laboratories Ltd.) was connected to an Agilent GC/MS system (GC: 7890A; MS: 5975C; MSD source: 230 °C; MS quadrupole: 150 °C; acquisition mode: scan; scanning range: $m/z$ = 10–550 after electron ionization (EI) at 70 eV; and split injection mode: 100:1). The experimental setup has been described elsewhere in more detail [25,26]. During the EGA-MS test, a sample (2.5–3.0 mg) was heated from 60 to 900 °C at a heating rate of 10 °C/min under He gas (103 ml/min) inside the pyrolyzer. Each test was done in triplicate. The generated products during pyrolysis were passed through a column (Ultra ALLOY® deactivated metal capillary tube UADTM (Frontier Laboratories Ltd.)) and measured by the MS. The inlet temperature and the GC oven were kept at 300 °C throughout the pyrolysis experiments. The measurement conditions were kept constant for all samples to allow for comparative interpretation of the results.

Water and $CO_2$ were monitored using the $m/z$ = 18 and 44 signals as molecular ions, respectively [17,27]. Levoglucosan is typically identified by $m/z$ = 60 which becomes the base peak when ionizing at 70 eV [25,28]. Minor contributions to $m/z$ = 60 from acetic acid and hydroxyacetaldehyde during cellulose pyrolysis were assumed to be negligible [14,28]. A semi-quantitative analysis of the production of water, $CO_2$, and levoglucosan was done by calculating the peak areas of their respective ions signal after normalizing by the sample mass (absolute intensity/sample mass). The relative production of the compounds was also calculated by dividing the peak area of the compounds by the peak area of the total ion chromatogram (TIC).

#### 2.3.2. Characterization of carbon fibers

The surface chemistry of the carbon fibers was evaluated via X-ray photoelectron spectroscopy (XPS), using an AXIS Ultra DLD electron spectrometer by Kratos Analytical (Manchester, U.K.). All experiments were performed with monochromatic Al Kα irradiation at 100W power and under neutralization. The fiber bundles were gently fixed on the sample holder with screws and a copper plate so that the part to be measured was left hanging outside the

holder. Each sample batch was pre-evacuated overnight to achieve stable ultra-high vacuum conditions. Furthermore, a fresh piece of Whatman filter paper was measured as an in-situ reference with each sample batch [29]. Experiments were performed on several locations for each sample. High-resolution spectra of carbon C 1s and N 1s regions were recorded for more detailed chemical analysis. Data were analyzed using CasaXPS software. The binding energies of the high-resolution spectra were calibrated by setting the C–O at 286.7 eV [30].

The chemical functionalities of the carbon fibers were investigated by Fourier transform infrared spectroscopy (FTIR) Nicolet6700 using a KBr method. The spectra were acquired from 64 scans, 4 $cm^{-1}$ resolution, and wavenumber range 4000–650 $cm^{-1}$.

The nanostructures of the carbon fiber were investigated by Raman spectroscopy and X-ray diffraction (XRD). The Raman spectra of the carbon fiber were collected using a LabRAM HR (HORIBA) equipped with a CCD detector. The samples were exposed to a 514 nm Ar laser for 60 s at 0.1% laser power (14 μW on the sample). Two scans were collected using a 100x microscope objective. Polarization of the incident laser was set by a half lambda plate to be parallel to the longitudinal direction of the carbon fibers. Baseline correction was applied to obtain a flat baseline between 800 and 2000 $cm^{-1}$. The peak at 1350 $cm^{-1}$ (*D* band) was fitted with a Lorentzian function, while the peak at 1590 $cm^{-1}$ (*G* Band) was fitted with a Breit-Wigner-Fano (BWF) function [31,32], which arguably can fit wide ranges of carbon [33]. The $I_D/I_G$ ratio was calculated from the height of the two peaks.

X-ray diffraction data of the carbon fiber were collected in the transmission mode setting of a CuKα X-ray instrument, SmartLab (RIGAKU) operated at 45 kV and 200 mA. The carbon fibers were fixed in the sample holder. The diffraction data were collected in a continuous mode from 5° to 60° $2\theta$ by $\theta/2\theta$ scan setting. The sample holder without sample was collected under the same experimental condition and was subtracted from the obtained scattering profiles of the samples. The subtracted data were smoothed using the Savitzky-Golay filter [34] with a window size of 29 and a polynomial order of 1. The smoothed data were then corrected for inelastic scattering.

The amorphous contribution was subtracted from the remaining elastic scattering profile using a smoothing procedure [35,36] applying a Savitzky-Golay filter from 6° to 55° $2\theta$ for each diffraction profile. Window size and polynomial order for the Savitzky-Golay filter were set to 201 (corresponding to 4° by $2\theta$) and 1, respectively. Iteration for the background estimation was repeated 200 times.

The background-corrected profiles were fitted with two pseudo-Voigt functions for (10) and (002) diffraction bands of carbon. The software lmfit [37] was used for the fitting. The apparent crystallite size (*CW hkl*) along the *a*-axis, *La,* was obtained from the (10) plane using the Scherrer equation (eq. (1)). Several terms such as extension in the in-plane aromatic clusters along the basal plane [38] or graphene sheets [38–40] have been used to described the increase in the apparent crystallite size along the *a*-axis *La*. In this study, in-plane aromatic cluster is synonymous for apparent crystallite size along the *a*-axis or graphene sheets.

$$CW_{hkl} = \frac{K\lambda}{\beta_{hkl}\cos\theta} \quad (1)$$

where λ is the X-ray wavelength, $\beta_{hkl}$ is the full width of half maximum (FWHM) of the diffraction peak in radians, $\theta$ is the diffraction angle of the peak, and shape factors of $K = 1.84$ for (10) band. The *d*-spacing of the (002) peak ($d_{002}$) was calculated via the Bragg equation:

$$d_{002} = \frac{n\lambda}{2\sin\theta} \quad (2)$$

TEM images of the nanostructure of the carbon fibers were recorded using a JEM 2100Plus TEM (JEOL Ltd., Japan) equipped with a Rio16 CMOS camera (Gatan Inc., USA) operated at 200 kV. Images were recorded with a relatively low accumulated dose value, 100-200 $e^-/Å^2$, using a low-dose procedure. The carbon fiber sample was ground by a mortar and then suspended in acetone. A small amount of the suspension was placed on a holey carbon grid and then air-dried prior to measurement [41]. Image analyses were done using the ImageJ software.

## 3. Results and discussion

### 3.1. Dehydration reaction and the production of levoglucosan during pyrolysis of composite fibers

As described in the introduction, promoting the dehydration reaction could reduce levoglucosan formation and increase the char yield. The common strategy to favor the dehydration reaction is to impregnate the substrate with dehydration catalysts such as Lewis acids or bases [42].

To elucidate the catalytic effect of chitosan on the heat-induced dehydration of cellulose, we monitored the formation of water and $CO_2$, which was shown to increase during catalytic dehydration [15,17]. In addition to the pure cellulose and the composite fibers, the physical mixtures of powdered cellulose fiber and chitosan powder were also investigated to distinguish interactions at different contact levels [21]. The extracted chromatograms of water and $CO_2$ are depicted in Fig. 1a and b, respectively. The total ion chromatogram (TIC) is also plotted in Fig. 1c. The water released below ~170 °C is physically desorbed from the fibers whereas above ~170 °C is likely associated with chemical reactions occurring during the pyrolysis process. This is consistent with earlier studies in which physical and chemical desorption was identified, although the exact temperature ranges might differ [43]. The peak maximum of released water and that of the TIC are all within a narrow temperature range, in line with the literature suggesting the water peak is located nearby the peak of overall mass loss [43,44].

The onset temperatures of the releases of water, $CO_2$, and TIC are presented in Fig. 2. Overall, there was a decrease in the onset temperature of the water released during the pyrolysis of composite fibers or physical mixtures from the standard cellulose fiber (Fig. 2a). Some studies described dehydration catalysts (e.g. organosilicones in combination with ammonium salts) shift the water release to lower temperatures in addition to increasing its total released amount [15,17]. However, even if there was some catalytic effect resulting from the interaction of the amine groups in chitosan and cellulose in the composite fiber, the shift of the onset temperature alone does not proof this. A downshift was also observed by the physical powder mixture, with pure chitosan powder degrading at a relatively low temperature (~200 °C) [45]. In contrast to the onset temperatures of water release, the onset temperatures of $CO_2$ and TIC of 25 wt% chitosan composite fiber were significantly lower than the neat cellulose fiber or physical mixtures (Fig. 2b and c, respectively). The onset temperatures of $CO_2$ and TIC of physical mixtures, on the other hand, were close to those of the neat cellulose fiber. The ~5 °C and ~10 °C downshift observed for $CO_2$ and TIC in the case of the 25 wt% chitosan composite fiber might be attributed to the catalytic activity of the chitosan in the composite fiber.

In an attempt to quantify the amount of released gasses, the peak area under the normalized intensity (peak area/mass) of water

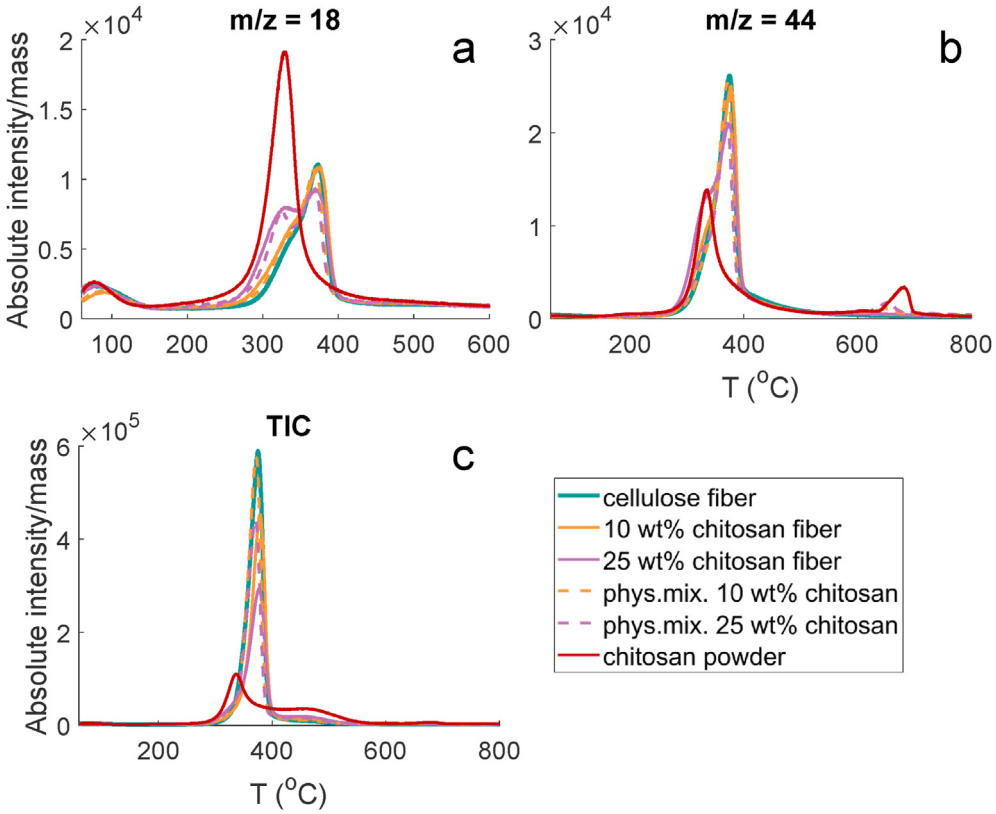


**Fig. 1.** Extracted chromatograms obtained during the pyrolysis of cellulose, composite fibers, physical mixture of chitosan and cellulose, and chitosan powder at 10 °C/min of water ($m/z = 18$) (a), $CO_2$ ($m/z = 44$) (b), and TIC (c). (A colour version of this figure can be viewed online.)

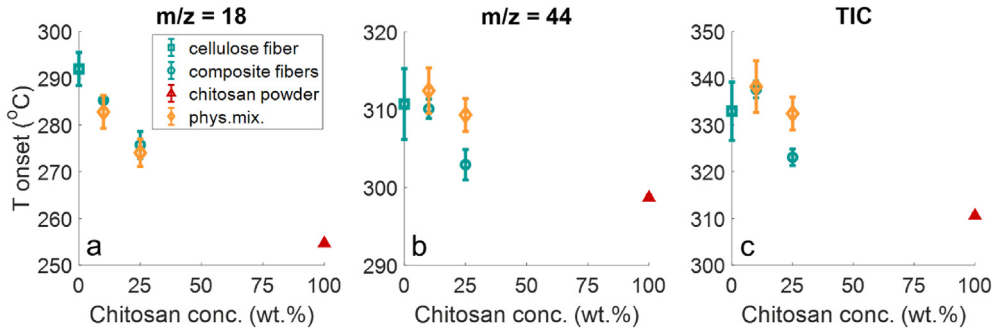


**Fig. 2.** Onset temperature from extracted chromatograms, calculated at 5% of peak area compared to total peak area at 170–400 °C, of water ($m/z = 18$) (a), $CO_2$ ($m/z = 44$) (b), and total ion chromatogram (TIC) (c). (A colour version of this figure can be viewed online.)

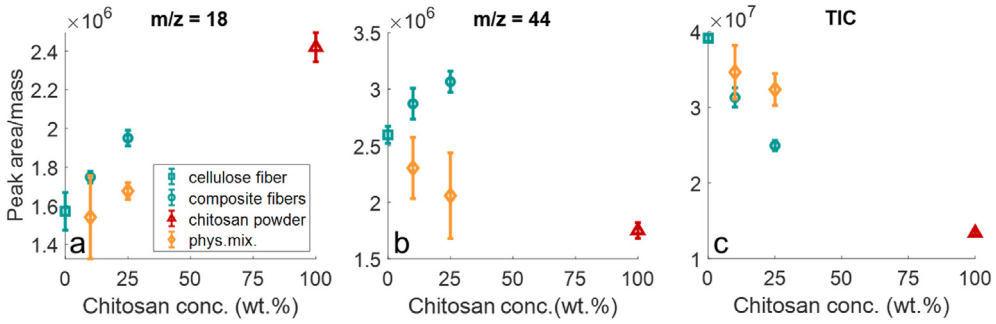


**Fig. 3.** Integrated EGA-MS peak areas, calculated from 170 to 400 °C, of water ($m/z = 18$) (a), $CO_2$ ($m/z = 44$) (b), and total ion chromatogram (TIC) (c) as a function of the chitosan share. (A colour version of this figure can be viewed online.)

and $CO_2$ from 170 to 400 °C was calculated (Fig. 3a and b). The temperature of 170 °C was chosen as a lower peak limit to account only for the pyrolysis water. The peak areas of water and $CO_2$ were significantly higher in the composite fibers than in the cellulose fiber. On the other hand, the signals of the physical powder mixtures were very close to the cellulose fiber. In particular, the 25 wt% chitosan composite fiber showed statistically significant higher values than the cellulose fiber and the corresponding physical mixture. Moreover, there are noticeable different trends (Fig. 3b) when comparing the peak area/mass of the $CO_2$ release between the composite fiber (rising trend) and the physical mixture (decreasing trend). Pure chitosan produced much less $CO_2$ (Fig. 3b). The decreasing trend of $CO_2$ in the physical mixtures with higher chitosan concentrations can simply be attributed to the lower amount of cellulose and higher amount of chitosan in the sample mixture. These results indicate that chitosan promotes the dehydration of cellulose when closely packed with cellulose at the nanoscale.

Besides the higher production of water and $CO_2$, the peak area of TIC of the 25 wt% chitosan composite fiber was significantly lower than the cellulose fiber or the corresponding physical mixture (Fig. 3c). This is in agreement with previous DTG results where the composite fibers had a lower degradation rate than the physical mixtures [21]. Considering that the TIC is representative of the released volatiles during pyrolysis, we normalized the peak area of water and $CO_2$ by the peak area of TIC calculated in the same temperature interval, as an indication of the relative water and $CO_2$ yield. Similar to the trend obtained for the peak area in Fig. 3, the peak area ratios shown in Fig. 4a and b indicate that the composite fibers produced larger amounts of water and $CO_2$ in the gas phase compared to the cellulose fibers and the powder mixtures. Again, the peak area ratio for the physical mixtures were very close to those obtained for the neat cellulose fibers.

The increased dehydration reaction and the higher yield of $CO_2$ indicate that the first pathway in cellulose pyrolysis as postulated by Shafizadeh was promoted in the composite fibers [13,22,46]. As expected, this led to a substantially lower formation of levoglucosan [14,21,47–49] than observed for the pure cellulose or physical mixtures, shown as peak area and peak area ratio in Fig. 5a and b, respectively. The enhanced dehydration during cellulose pyrolysis was reported to produce cross-linked structures with enhanced thermal stability, lowering levoglucosan and boosting char formation [46,50–52]. These results are in line with our previous study that indicated a catalytic effect of chitosan on the thermal degradation of cellulose shown by the increased carbon yield [21]. It also confirms that such catalytic effect or synergistic interaction is only enabled when chitosan and cellulose are in intimate contact created through co-dissolution and coagulation as opposed to a simple physical powder mixture of both biopolymers.

### 3.2. Nanostructure of carbon fibers derived from the composite fibers

The carbonized fibers in this study were produced at three temperatures: 500, 700, and 900 °C. The gradual development of the nanostructure of the carbon fibers in this temperature range was studied using the complementary methods of Raman spectroscopy and XRD (Fig. 6). However, due to the moderate temperature ranges and finite number of samples, cautious interpretation of the structural properties of the carbon fibers derived from cellulose and chitosan-composite fibers is required.

Raman spectroscopy is a widely used tool to characterize the structure of carbon materials using two characteristic bands (*D* and *G* bands) [53]. The appearance of the *G* band (~1500-1630 $cm^{-1}$) is due to the in-plane bond-stretching of pairs of $sp^2$ atoms both in chains or ring structures [33]. The *D* band (~1350 $cm^{-1}$) only emerges when there are ring structures as it is derived from the breathing mode of sixfold aromatic rings [33]. The intensity ratio of the *D* and *G* bands $I_D/I_G$ is commonly used to follow the evolution of the nanostructures of the carbon materials as it is connected to the size of the in-plane aromatic cluster *La* [33,38,54]. For highly ordered carbons, for example highly oriented graphite, the presence of "disorders" reduces the in-plane cluster size *La* and increases the intensity of the *D* band, and consequently the $I_D/I_G$ ratio [33]. For such a system, the Tuinstra-Koenig (TK) equation [54] is valid. However, for highly disordered carbons with smaller *La* (typically below 40-20 Å) [55], the intensity of the *D* band is mainly connected to the probability to find aromatic rings of the size of the aromatic clusters [33]. Therefore, for this regime, equation (3) proposed by Ferrari and Robertson [33] is favored to derive *La* from $I_D/I_G$ when using Lorentzian and BWF functions to fit the *D* and *G* bands, respectively [38]. In this study, we adopted equation (3) to estimate *La* derived from $I_D/I_G$, called *La(Raman)*, considering the relatively low carbonization temperature in our experimental condition and thus the still highly disordered system [56].

$$La(Raman) = \left[\left(\frac{ID}{IG}\right) \Big/ 0.0055\right]^{1/2} \text{Å} \quad (\text{forlaserwavelengthof514.5nm}) \tag{3}$$

The $I_D/I_G$ ratio of the carbon fibers derived from the chitosan-cellulose composite fibers is shown in Fig. 6a. The increase of the

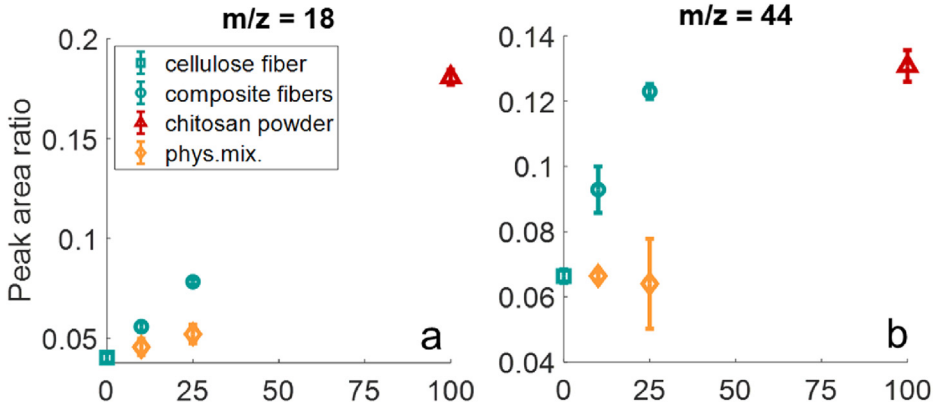


**Fig. 4.** Peak area ratio (= peak area of a specific *m*/*z* divided by the total TIC peak area calculated from 170 to 400 °C at 10 °C/min) during pyrolysis of cellulose fiber, composite fibers, physical mixture of chitosan and cellulose, and chitosan powder of water (*m*/*z* = 18) (a) and $CO_2$ (*m*/*z* = 44) (b). (A colour version of this figure can be viewed online.)

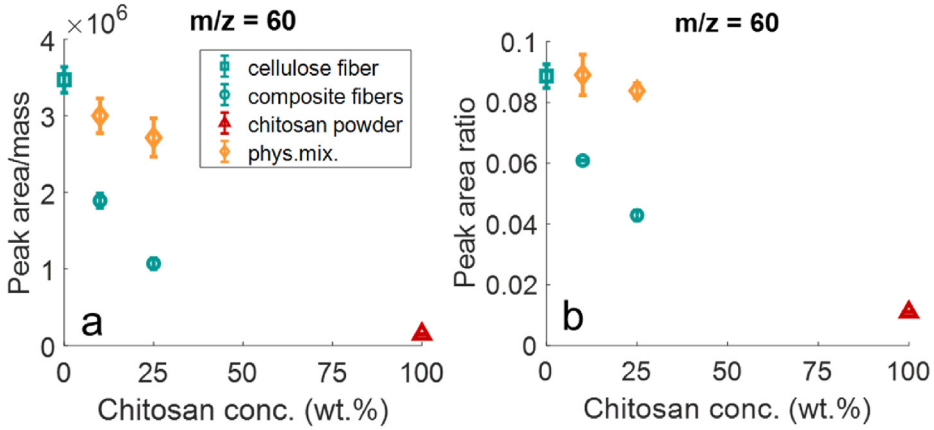


**Fig. 5.** Peak area (a) and the peak ratio of $m/z = 60$ (as described in Fig. 4) (b) as an indicator of levoglucosan formation during pyrolysis of the cellulose fiber, composite fibers, physical mixture of chitosan and cellulose, and chitosan powder at 10 °C/min heating rate. (A colour version of this figure can be viewed online.)

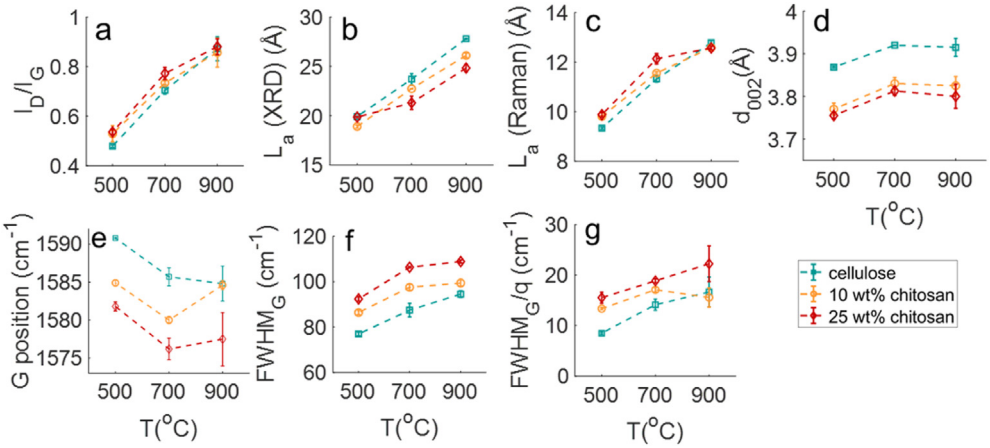


**Fig. 6.** $I_D/I_G$ ratio (a), *La* from XRD (b), *La* from Raman (c), $d_{002}$ (d), the position of the *G* peak (e), $FWHM_G$ (f), and $FWHM_G/q$ (g) of the carbon fibers derived from cellulose and composite fibers as a function of pyrolysis temperature. (A colour version of this figure can be viewed online.)

pyrolysis temperature from 500 to 900 °C led to an expected increase in the $I_D/I_G$ ratio from ~0.5 to ~0.8, suggesting a growth in the in-plane aromatic clusters [33,38]. This agreed well with XRD results presented in Fig. 6b showing a rise in the apparent crystallite size along the basal plane *La(XRD)* within the same temperature range. This observation is in line with a number of studies that have reported an increase in the $I_D/I_G$ ratio as well as the associated in-plane aromatic domains from biomass-derived pyrolytic carbon such as wood and bark [57,58], cellulose fibers [59–61], and kraft-lignin fibers [62] with increasing carbonization temperatures. The growth of the aromatic carbons with increasing pyrolysis temperature is also indicated in the C 1s spectra of the XPS analyses in Fig. S1.

Comparing *La(XRD)* in Fig. 6b with *La(Raman)* in Fig. 6c, it is shown that *La(Raman)* were about half of *La(XRD)*. Cuesta et al. discussed this discrepancy already earlier [63]. XRD measurements average any preferred orientation of microcrystals in randomly distributed particles while Raman probes only a limited volume of the particle surface [63]. As the XRD method is more preferable when measuring *La* [63], the *La(XRD)* values in Fig. 6b were used to estimate the size of the in-plane aromatic clusters in this study.

Besides the increase in *La,* the XRD measurement revealed that there was an increase in the apparent interlayer distance of the aromatic planes $d_{002}$ from 500 to 700 °C (~3.77–3.90 Å), plotted in Fig. 6d. The increase in $d_{002}$ from 500 to 700 °C could reflect an increase in the topological disorders of the in-plane aromatic cluster [63,64]. In addition to the $d_{002}$ measured by XRD [63,64], in-plane disorders of the aromatic clusters can be evaluated by Raman parameters, such as the full width half maximum of the *D* and *G* band ($FWHM_D$ and $FWHM_G$, respectively) [38,65,66]. In this study, only the *G* band was utilized because a combination of Lorentzian-BWF fitting was applied, in which the *D* band is the least accurate for amorphous carbon as described by Ferrari and Robertson [33]. The *G* band, on the other hand, is always present in any carbon material at any excitation energy with a best-defined peak shape [67]. The *G* peak position is linked to the bond strength while $FWHM_G$ reflects the bond length and angle distortions, hence, they can reflect the ordering of the in-plane aromatic clusters [31–33,38,68]. Additionally, the $FWHM_G/q$ ($q$ is the coupling coefficient in asymmetric BWF fitting) value approaching 0 indicates the completion of in-plane (two-dimensional) ordering and the commencement of the stacking (three-dimensional) ordering [38,66]. The in-plane disorder in the sixfold aromatic cluster includes disorders that hinders flattening or extension of the basal planes [31,38]. The upshift of the *G* band peak and reduced $FWHM_G$ and $FWHM_G/q$ values indicate an increase in the ordering of the in-plane sixfold aromatic clusters [31,38,66,68]. Therefore, the downshift of the *G* peak position and the rise in the $FWHM_G$ and

$FWHM_G/q$, in Fig. 6e, f, and 6g, respectively, from 500 to 700 °C could indicate an increase in the in-plane disorders of aromatic clusters, in-line with the increase in disorders shown by $d_{002}$.

One of the reasons of the increase in the in-plane disorders exhibited by $d_{002}$ in Fig. 6d and Raman parameters in Fig. 6e, f, and 6g, respectively, from 500 to 700 °C might be due to heteroatoms, particularly nitrogen incorporation into the carbon scaffold. Based on elemental analysis (EA) results, the nitrogen originating from chitosan was largely retained in the carbon structure: the N/C-ratio of the 25 wt% chitosan composite fiber went from originally ~0.031 to ~0.046 after pyrolysis at 700 °C [21]. Nitrogen has several effects on the carbon structure, including the formation of energetically more favored non-hexagonal (i.e. pentagon) rings within the basal planes [38,69–72], which can contribute to the topological disorders of aromatic planes [56,73–75]. Besides nitrogen, other heteroatoms such as oxygen were reported to induce non-hexagonal cycles in sixfold aromatic planes [40,55,56]. In a study using the atomic pair distribution function analysis with neutron scattering data by Petkov et al. [40], "curved and somewhat defective graphene sheets" were produced from pyrolysis of oxygen-rich poly(furfuryl alcohol) at 800 °C, suggesting a topological disorders induced by oxygen containment in the precursor fiber. In addition, Paris et al. 2005 reported that the increase in the $d_{002}$ of spruce normal wood occurred at pyrolysis temperatures from ~430 to ~630 °C and that the decrease in the $d_{002}$ started at temperatures higher than ~1000 °C. These studies support the observed increase in the in-plane disorders shown by the rising $d_{002}$ at 500–700 °C from our precursor fibers which are rich in both nitrogen and oxygen [21].

At pyrolysis temperature from 700 to 900 °C, the development of $d_{002}$ was relatively stagnant (Fig. 6d), suggesting a comparatively unchanged topological ordering of the aromatic cluster compared to that at 500–700 °C. The elemental analysis also showed only small changes in the nitrogen and oxygen content (N/C and O/C, respectively, in mol/mol) of the carbon when advancing from 700 to 900 °C compared to 500–700 °C [21], supporting the picture of the smaller change in the in-plane ordering exhibited by $d_{002}$. Despite this, general trends from Raman parameters ($G$ peak, $FWHM_G$, and $FWHM_G/q$) at 700–900 °C were difficult to extract and some values suffer from a high standard deviation (Fig. 6e, f, and 6g, respectively). These results support the conclusion from Cuesta et al. that information from XRD and Raman techniques are not equivalent but complementary and that some disorders, depending on the origin of the disorders, are reflected only in $d_{002}$ but not in the Raman parameter ($R = I_D/I_D + I_G$) and vice versa [63].

The continuous increase in the size of the aromatic clusters *La(XRD)* at 500–900 °C was accompanied by a simultaneous increase in topological disorder indicated by the rising $d_{002}$, which occurred particularly from 500 to 700 °C. Similar observations were reported by others earlier. Abrasonis et al. [38] compared several methods for growing amorphous carbon nitride ($CN_x$) thin films at low temperatures (≤450 °C) with low *La* (<20 nm) and with varying nitrogen content (~1–20 at.%) and reported that some specific methods could produce carbon with both larger cluster sizes and higher degree of disorder in sixfold clusters than the other methods. Paris et al. reported that the carbonization of spruce wood, *i.e.* oxygen-rich lignocellulosic material, resulted in a simultaneous increase of *La* (~2.50 nm to ~2.85 nm) and $d_{002}$ (~0.388 nm to ~0.394 nm) in the moderate temperature range from ~430 °C to ~630 °C. Lastly, Kim et al. [76] showed that there was an increase of both *La* and $d_{002}$ (from 2.540 to 2.959 nm and from 0.3756 to 0.3765 nm, respectively), when stabilized pitch fibers were pyrolyzed from 800 to 900 °C. The pyrolysis of pitch powder at the same temperature range showed similar trends, where $d_{002}$ increased from 0.3455 to 0.3462 nm and *La* from 3.319 to 4.048 nm. The stabilized pitch fiber was produced from pitch powder; the difference was that the "fibers suffered some shear stress during the melt-blowing process and had a high oxygen content from the stabilization process", explaining the higher $d_{002}$ of the carbon from the pitch fibers as compared to the pitch powder. These studies imply that the simultaneous increase in *La* and $d_{002}$ could occur concurrently depending on the growth mechanism and type of precursor (e.g. heteroatom content), particularly at a temperature range below 900 °C as in our study.

As discussed earlier, the precursor fibers in this study contain nitrogen besides oxygen. The elemental analysis of our and other studies [21,77,78] have shown that nitrogen is volatilized to a much lesser extent compared to oxygen during pyrolysis below 1000 °C. Thus, the effect of nitrogen on the evolution of the carbon structure has to be taken into account.

Besides the formation of non-hexagonal rings, Abrasonis et al. [38] have summarized other effects of nitrogen on carbon structures, including (i) substitution of carbon atoms in in-plane aromatic clusters and extension of $sp^2$ cluster [66,79,80], (ii) occupation of pyridine-like or nitrile-like configurations that can terminate the growth of in-plane aromatic clusters cluster [66,79,81], and (iii) formation of cross-links between adjacent planes [75,82,83].

To study the effect of the nitrogen present in the precursor fiber on the carbon nanostructure, the XRD- and Raman-derived parameters are plotted against chitosan concentration in the precursor fibers (Fig. 7).

The increasing nitrogen content caused a reduction of *La* at higher temperatures (700 and 900 °C) (Fig. 7a), whereas at 500 °C the effect of nitrogen on *La* seemed negligible. The difference of *La* between carbon fibers from standard cellulose fiber and 25 wt% chitosan was ~2.98 and ~2.43 Å for the carbonization at 900 and 700 °C, respectively. In a study of carbon nitride films grown by ion beam sputtering [38], the higher nitrogen content reduced the *La* of the carbon grown at 450 °C but did not give clear effects on *La* at 150 and 300 °C. Although the authors used a different production method, their study and the current study indicate that the effect of nitrogen on the carbon structure also depends on the production temperature [84]. This temperature dependency could explain the different trends of *La* at different pyrolysis temperatures in Fig. 7a. The reduction in *La* at high carbonization temperatures was attributed to nitrogen atoms occupying the cluster edges, forming pyridine-like or nitrile-like configurations, and consequently suppressed the temperature-induced cluster growth [38].

The formation of the pyridine-like configurations at higher pyrolysis temperatures (700 and 900 °C) is also found in the XPS N 1s spectrum of carbon fiber derived from 25 wt% chitosan composite fibers (Fig. 8). It should be noted that the intensity of the N 1s was relatively weak throughout all spectra. Thus, any fitting result must be interpreted with caution since the choice of the number of functions and the location of their peak maxima inherently affects the result. For the carbon fiber pyrolyzed at 500 °C, the N 1s peak showed two main peaks at ~399.2 ± 0.1 eV and ~400.4 ± 0.2 eV. The peak at ~399.2 eV represented aminic configuration [23,85]. The presence of the aminic group was also confirmed via FTIR spectroscopy by the N–H stretching band in the range of 3300–3450 $cm^{-1}$ [86] in Fig. S2a. The peak at ~400.4 eV could be assigned to pyrrole-like nitrogen [87,88]. At 700 °C, the XPS intensity of aminic nitrogen decreased whereas a new peak appeared at ~398.3 ± 0.1 eV which corresponds to pyridinic configuration [88–90]. The peak representing pyrrolic nitrogen was still present at this temperature. At 900 °C, the nitrogen modification remained mostly pyridinic (~398.2 eV) and pyrrolic (~400.6 eV) as already observed at 700 °C. The presence of five-membered rings from the pyrrolic nitrogen which contributed to the topological disorder of

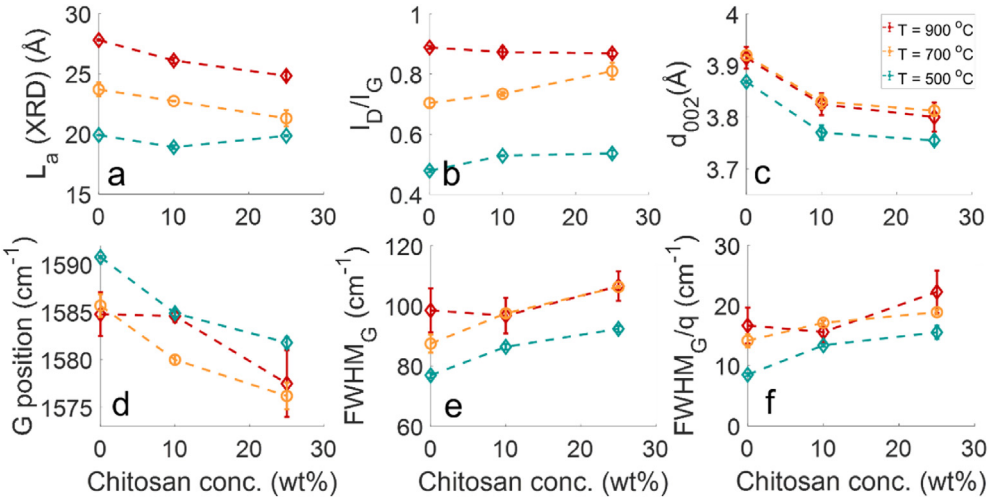


**Fig. 7.** *La* (XRD) (a), $I_D/I_G$ ratio (b), $d_{002}$ (c), position of the *G* peak (d), $FWHM_G$ (e), and $FWHM_G/q$ (f) of carbon fibers as a function of chitosan concentration in the respective precursor composite fiber. (A colour version of this figure can be viewed online.)

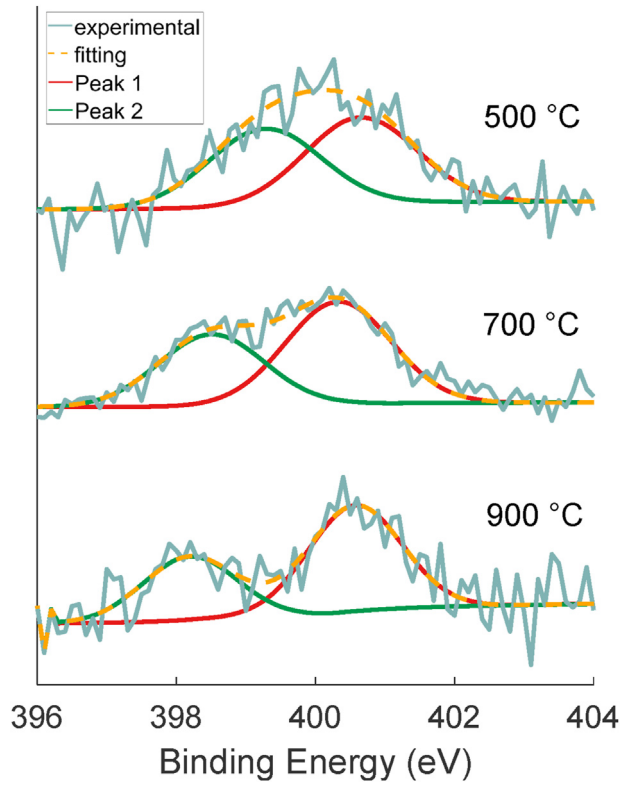


**Fig. 8.** XPS N 1s spectra of carbon fiber derived from 25 wt% chitosan composite fiber at different pyrolysis temperatures. (A colour version of this figure can be viewed online.)

the in-plane aromatic clusters discussed previously is supported by the XPS result.

Compared to the effect of the pyrolysis temperatures on *La* (Fig. 6b), the effect of nitrogen from chitosan on *La* (Fig. 7a) was much lower, and hence, the changes in $I_D/I_G$ due to nitrogen (Fig. 7b) were less pronounced. Besides the slight decrease in *La* (Fig. 7a), the $d_{002}$ values of the carbon fibers derived from the chitosan-containing composite fibers were lower than in the reference cellulose fiber (Fig. 7c). The shorter interlayer distance $d_{002}$ in the nitrogen-containing carbon material was also visible in TEM images (Fig. 9). The fringes of aromatic layers are visible in both samples derived from the cellulose and composite fiber. Radial profiles of the FFT 2D power spectra (Fig. 9c) show relatively broad peaks at around 2.5 $nm^{-1}$, corresponding to the interlayer spacing, $d_{002}$. The peak position of the composite fiber shifts slightly compared to that of the cellulose fiber, from 2.56 $nm^{-1}$ to 2.66 $nm^{-1}$, that equals to a decrease in $d_{002}$ from 3.9 Å to 3.8 Å.

Despite the different initial N/C ratios in the 10 and 25 wt% chitosan composite fiber (~0.012 and ~0.031, respectively), the $d_{002}$ values of the respective carbon materials did not differ significantly (Fig. 7c). This suggests that minor doping with nitrogen-containing compounds could already induce structural changes in the resulting carbon [38,69,91]. A similar trend is observed in the XPS N 1s spectra (Fig. 10). The nitrogen in carbon derived from 10 to 25 wt% chitosan composite fibers pyrolyzed at 900 °C is mostly present as pyridinic (~398.3 ± 0.1 eV) and pyrrolic moieties (~400.4 ± 0.2 eV).

The decrease in $d_{002}$ with chitosan addition in the precursor fiber could suggest a decrease in the topological disorders in the in-plane aromatic clusters. However, from Fig. 7d, e, and 7f, respectively, there was a downshift of the *G* peak and an increase in both the $FWHM_G$ and the $FWHM_G/q$ with increasing nitrogen content up to 25 wt%, indicating rising in-plane disorder in the aromatic clusters caused by the incorporated nitrogen atoms [92]. The presence of five-membered heterocycles in the pyrrolic units exhibited in the XPS of the carbon derived from 10 to 25 wt% chitosan (Fig. 10) could reasonably explain the topological disorders of the in-plane aromatic clusters. Therefore, the decrease in the $d_{002}$ by the nitrogen inclusion was not due to the flattening induced by a more topological ordering of the basal planes [64]. Again, this result further supports that information from XRD and Raman techniques cannot be treated as equivalent but rather complementary [63]. Depending on the cause of disorders, some disorders are reflected only in $d_{002}$ but not in *R* and vice versa [63], as discussed previously. Furthermore, Lespade et al. [93] suggested that first-order Raman spectra only correlate with the two-dimensional order or in-plane direction of the aromatic clusters but not with the three-dimensional/stacking ordering. Thus, the combination of complementary analytical techniques is needed to describe the properties (e.g. ordering) of materials adequately.

As previously mentioned, incorporated nitrogen does not only cause in-plane disorders but can also induce cross-links [75,82,83].

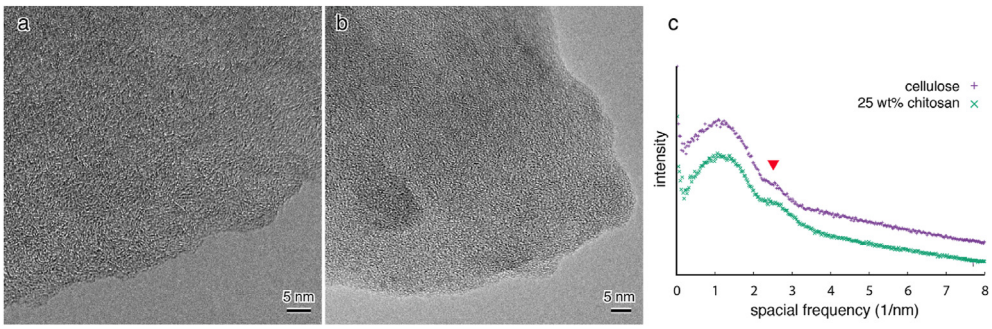


**Fig. 9.** High-resolution images of carbon fibers pyrolyzed at 900 °C from cellulose (a) and 25 wt% chitosan-containing composite fibers (b); radial profiles of FFT power spectra of the two samples derived from the cellulose (purple) and the composite fibers (c). Red arrowhead indicates the intensity peaks corresponding to the spacing of aromatic layers. (A colour version of this figure can be viewed online.)

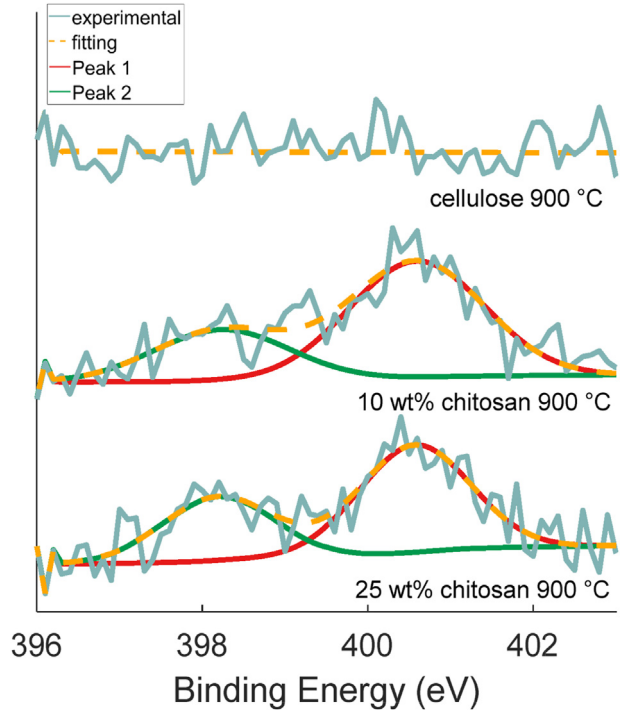


**Fig. 10.** XPS N 1s spectra of carbon fiber at 900 °C derived from cellulose, 10 and 25 wt % chitosan-containing composite fibers as indicated in the graph. (A colour version of this figure can be viewed online.)

The smaller apparent interlayer spacing $d_{002}$ exhibited by the nitrogen-containing carbon fibers might be due to the formation of interplanar cross-links [94]. Several mechanisms for the formation of cross-links in the basal planes have been proposed [95]. Nitrogen can increase the flexibility of the carbon skeleton when forming cross-links during the stabilization process of PAN fiber [96]. Also, nitrogen can become a radical source for the adjacent carbon matrix, enabling cross-linking at carbon atoms [71,95,97]. Additional covalent bonds can form at olefine entities through propagation by nitrogen radicals [95]. Moreover, pentagon rings induced by nitrogen can cause buckling of the basal planes, facilitating covalent bond formation between planes [75,84]. This might also be a reason for the observed in-plane cluster disorders indicated by the downshift of the *G* peak and the rise in $FWHM_G$ and $FWHM_G/q$ with higher nitrogen incorporation previously (Fig. 7d, e, and 7f).

The formation of the cross-link structures in the chitosan-derived carbon fibers has been suggested in Chapter 3.1 where its formation was associated with an enhanced dehydration reaction, the higher thermal stability of the char, and lower volatile releases during pyrolysis [46,50–52,98]. Moreover, the carbon fibers derived from chitosan-cellulose composite fibers showed higher tensile strength and Young's Modulus compared to those derived from the standard cellulose fibers [21], despite the in-plane (two-dimensional) disorder in the aromatic planes indicated by the Raman parameters presented here. Similar observations on simultaneous development of cross-linking, mechanical properties, and surface defects have also been reported in another study [99]. This highlights the importance of a holistic assessment to construct structure-property relationships [94,98–100].

## 4. Conclusion

The results in this study confirm that chitosan in chitosan-cellulose composite fibers catalyzes the dehydration reaction which results in lower carbonaceous volatiles and higher carbon yields. It is important to highlight that the catalytic activity is only observed when chitosan was in intimate contact with cellulose at a nanoscale level in the composite fiber, as there was an insignificant change in the cellulose degradation behavior exhibited by the simple physical powder mixture. A more detailed investigation of other compounds volatilized during pyrolysis of cellulose with further additives will be provided in the next study to gain a deeper understanding of the alteration of the cellulose pyrolysis mechanism in the presence of chitosan and other nitrogen containing polymers. Pyrolysis of the pure cellulose and the composite fibers in the temperature range of 500–900 °C increased the size of the aromatic clusters. Nitrogen present in chitosan was suggested to contribute to the evolving in-plane disorder of the aromatic clusters. The experimental results also suggest that the presence and location of nitrogen could be responsible for shortening the inter-graphene spacing, possibly by promoting the formation of cross-linking structural elements. The formation of cross-links is associated with the catalytically enhanced dehydration reaction and the improvement of the mechanical properties of the resulting carbon fibers. The carbon yield and the mechanical properties of cellulose-derived carbon fibers were increased by the sole use of another abundant biopolymer, which has direct implications on the potential and economic feasibility of carbon fibers derived from renewables. These improvements can make chitosan-cellulose composite fibers also attractive as precursors of carbon materials for other applications. Pyrolyzing the composite fibers at suitable temperatures could be a simple strategy to tailor the properties of the nitrogen-doped carbon matrix for the desired applications, such as chemical or electrochemical catalysts.

## CRediT authorship contribution statement

**Hilda Zahra:** Conceptualization, Methodology, Visualization, Writing – original draft, Writing – review & editing, experiments of spinning of cellulose & chitosan-cellulose composite fibers and subsequent carbonization; experiments and formal analysis of EGA-MS, Raman, XRD, FTIR, XPS. **Daisuke Sawada:** Methodology, Formal analysis, of EGA-MS, XRD, and Raman, Writing – review & editing. **Shogo Kumagai:** Methodology, Formal analysis, of EGA-MS, Writing – review & editing. **Yu Ogawa:** Writing – review & editing, experiment of TEM and formal analysis. **Leena-Sisko Johansson:** Writing – review & editing, experiment of XPS and formal analysis. **Yanling Ge:** Writing – review & editing, experiment of TEM and formal analysis. **Chamseddine Guizani:** Writing – review & editing. **Toshiaki Yoshioka:** Writing – review & editing. **Michael Hummel:** Funding acquisition, Resources, Writing – review & editing.

## Declaration of competing interest

The authors declare that they have no known competing financial interests or personal relationships that could have appeared to influence the work reported in this paper.

## Acknowledgements

This project has received funding from the European Research Council (ERC) under the European Union's Horizon 2020 research and innovation program (grant agreement No 715788). HZ gratefully acknowledges The Finnish Foundation for Technology Promotion, Jenny and Antti Wihuri Foundation, and Niemi Foundation for the encouragement grants. The authors gratefully acknowledge: OtaNano-Nanomicroscopy Center (Aalto-NMC) for the use of XRD instruments; OtaNano-Low Temperature Laboratory (Aalto-LTL) for the use of Raman instrument; Graduate School of Environmental Studies (GSES) of Tohoku University for the use of the EGA-MS and FTIR instruments. YO thanks the NanoBio-ICMG platform (FR 2607) for granting access to the electron microscopy facility. HZ thanks Kanako Yamada and Daichi Ikuta for the support during EGA-MS measurements.

## Appendix A. Supplementary data

Supplementary data to this article can be found online at https://doi.org/10.1016/j.carbon.2021.08.062.

## References

[1] V.K. Gupta, P.J.M. Carrott, R. Singh, M. Chaudhary, S. Kushwaha, Cellulose: a review as natural, modified and activated carbon adsorbent, Bioresour. Technol. 216 (2016) 1066–1076.
[2] T. Zhang, L. Yang, X. Yan, X. Ding, Recent advances of cellulose-based materials and their promising application in sodium-ion batteries and capacitors, Small 14 (47) (2018), 1802444-1 - 1802444-20.
[3] M.L. Foresti, A. Vázquez, B. Boury, Applications of bacterial cellulose as precursor of carbon and composites with metal oxide, metal sulfide and metal nanoparticles: a review of recent advances, Carbohydr. Polym. 157 (2017) 447–467.
[4] E. Guilminot, F. Fischer, M. Chatenet, A. Rigacci, S. Berthon-Fabry, P. Achard, et al., Use of cellulose-based carbon aerogels as catalyst support for PEM fuel cell electrodes: electrochemical characterization, J. Power Sources 166 (1) (2007) 104–111.
[5] L.F. Chen, Z.H. Huang, H.W. Liang, H.L. Gao, S.H. Yu, Three-dimensional heteroatom-doped carbon nanofiber networks derived from bacterial cellulose for supercapacitors, Adv. Funct. Mater. 24 (32) (2014) 5104–5111.
[6] Z. Gao, C. Bumgardner, N. Song, Y. Zhang, J. Li, X. Li, Cotton-textile-enabled flexible self-sustaining power packs via roll-to-roll fabrication, Nat. Commun. 7 (1) (2016) 1–12.
[7] Z. Gao, Y. Zhang, N. Song, X. Li, Towards flexible lithium-sulfur battery from natural cotton textile, Electrochim. Acta 246 (2017) 507–516.
[8] Z. Gao, N. Song, Y. Zhang, X. Li, Cotton-textile-enabled, flexible lithium-ion batteries with enhanced capacity and extended lifespan, Nano Lett. 15 (12) (2015) 8194–8203.
[9] Z. Gao, N. Song, Y. Zhang, X. Li, Cotton textile enabled, all-solid-state flexible supercapacitors, RSC Adv. 5 (20) (2015) 15438–15447.
[10] A.G. Dumanlı, A.H. Windle, Carbon fibres from cellulosic precursors: a review, J. Mater. Sci. 47 (10) (2012) 4236–4250.
[11] Y. Wu, Y. Zhao, H. Wang, F. Zhang, R. Li, J. Xiang, et al., Ambient reductive synthesis of N-heterocyclic compounds over cellulose-derived carbon supported Pt nanocatalyst under H 2 atmosphere, Green Chem. 22 (12) (2020) 3820–3826.
[12] S. Suganuma, K. Nakajima, M. Kitano, D. Yamaguchi, H. Kato, S. Hayashi, et al., Synthesis and acid catalysis of cellulose-derived carbon-based solid acid, Solid State Sci. 12 (6) (2010) 1029–1034.
[13] F. Shafizadeh, Introduction to pyrolysis of biomass, J. Anal. Appl. Pyrol. 3 (4) (1982) 283–305.
[14] M. Statheropoulos, S.A. Kyriakou, Quantitative thermogravimetric-mass spectrometric analysis for monitoring the effects of fire retardants on cellulose pyrolysis, Anal. Chim. Acta 409 (1–2) (2000) 203–214.
[15] H. Li, Y. Yang, Y. Wen, L. Liu, A mechanism study on preparation of rayon based carbon fibers with (NH4) 2SO4/NH4Cl/organosilicon composite catalyst system, Compos. Sci. Technol. 67 (13) (2007) 2675–2682.
[16] P.H. Brunner, P.V. Roberts, The significance of heating rate on char yield and char properties in the pyrolysis of cellulose, Carbon 18 (3) (1980) 217–224.
[17] Q. Wu, N. Pan, K. Deng, D. Pan, Thermogravimetry–mass spectrometry on the pyrolysis process of Lyocell fibers with and without catalyst, Carbohydr. Polym. 72 (2) (2008) 222–228.
[18] V. Mamleev, S. Bourbigot, J. Yvon, Kinetic analysis of the thermal decomposition of cellulose: the main step of mass loss, J. Anal. Appl. Pyrol. 80 (1) (2007) 151–165.
[19] S. Maduskar, V. Maliekkal, M. Neurock, P.J. Dauenhauer, On the yield of levoglucosan from cellulose pyrolysis, ACS Sustain. Chem. Eng. 6 (5) (2018) 7017–7025.
[20] A. Broido, Thermogravimetric and differential thermal analysis of potassium bicarbonate contaminated cellulose, Pyrodynamics 4 (1966) 243–251.
[21] H. Zahra, D. Sawada, C. Guizani, Y. Ma, S. Kumagai, T. Yoshioka, et al., Close packing of cellulose and chitosan in regenerated cellulose fibers improves carbon yield and structural properties of respective carbon fibers, Biomacromolecules 21 (2020) 4326–4335.
[22] A. Pappa, K. Mikedi, N. Tzamtzis, M. Statheropoulos, Chemometric methods for studying the effects of chemicals on cellulose pyrolysis by thermogravimetry–mass spectrometry, J. Anal. Appl. Pyrol. 67 (2) (2003) 221–235.
[23] M. Inagaki, M. Toyoda, Y. Soneda, T. Morishita, Nitrogen-doped carbon materials, Carbon 132 (2018) 104–140.
[24] S.K. Singh, K. Takeyasu, J. Nakamura, Active sites and mechanism of oxygen reduction reaction electrocatalysis on nitrogen-doped carbon materials, Adv. Mater. 31 (13) (2019), 1804297-1 - 1804297-17.
[25] A. Watanabe, C. Watanabe, R.R. Freeman, N. Teramae, H. Ohtani, Hydrogenation reactions during pyrolysis-gas chromatography/mass spectrometry analysis of polymer samples using hydrogen carrier gas, Anal. Chem. 88 (10) (2016) 5462–5468.
[26] S. Kumagai, S. Motokucho, R. Yabuki, A. Anzai, T. Kameda, A. Watanabe, et al., Effects of hard-and soft-segment composition on pyrolysis characteristics of MDI, BD, and PTMG-based polyurethane elastomers, J. Anal. Appl. Pyrol. 126 (2017) 337–345.
[27] K. Kasataka, S. Kumagai, T. Kameda, Y. Saito, T. Yoshioka, Enhancement of gasification and liquefaction during fast co-pyrolysis of cedar wood and polyethylene through control of synergistic interactions, Bioresource Technology Reports 11 (2020), 100431-1 - 100431-8.
[28] A.D. Pouwels, G.B. Eijkel, J.J. Boon, Curie-point pyrolysis-capillary gas chromatography-high-resolution mass spectrometry of microcrystalline cellulose, J. Anal. Appl. Pyrol. 14 (4) (1989) 237–280.
[29] L.S. Johansson, J.M. Campbell, O.J. Rojas, Cellulose as the in situ reference for organic XPS. Why? Because it works, Surf. Interface Anal. 52 (2020) 1134–1138.
[30] G. Beamson, High Resolution XPS of Organic Polymers, The Scienta ESCA 300 Database, 1992.
[31] D.G. McCulloch, S. Prawer, A. Hoffman, Structural investigation of xenon-ion-beam-irradiated glassy carbon, Phys. Rev. B 50 (9) (1994) 5905–5917.
[32] D.G. McCulloch, S. Prawer, The effect of annealing and implantation temperature on the structure of C ion-beam-irradiated glassy carbon, J. Appl. Phys. 78 (5) (1995) 3040–3047.
[33] A.C. Ferrari, J. Robertson, Interpretation of Raman spectra of disordered and amorphous carbon, Phys. Rev. B 61 (20) (2000) 14095–14107.
[34] A. Savitzky, M.J.E. Golay, Smoothing and differentiation of data by simplified least squares procedures, Anal. Chem. 36 (8) (1964) 1627–1639.
[35] S. Brückner, Estimation of the background in powder diffraction patterns through a robust smoothing procedure, J. Appl. Crystallogr. 33 (3) (2000) 977–979.
[36] K. Frost, D. Kaminski, G. Kirwan, E. Lascaris, R. Shanks, Crystallinity and structure of starch using wide angle X-ray scattering, Carbohydr. Polym. 78 (3) (2009) 543–548.
[37] M. Newville, T. Stensitzki, D.B. Allen, M. Rawlik, A. Ingargiola, A. Nelson, LMFIT: non-linear least-square minimization and curve-fitting for Python,

Astrophysics Source Code Library (2016).
[38] G. Abrasonis, R. Gago, M. Vinnichenko, U. Kreissig, A. Kolitsch, W. Möller, Sixfold ring clustering in s p 2-dominated carbon and carbon nitride thin films: a Raman spectroscopy study, Phys. Rev. B 73 (12) (2006), 125427-1-125427-13.
[39] O. Paris, C. Zollfrank, G.A. Zickler, Decomposition and carbonisation of wood biopolymers—a microstructural study of softwood pyrolysis, Carbon 43 (1) (2005) 53–66.
[40] V. Petkov, R.G. DiFrancesco, S.J.L. Billinge, M. Acharya, H.C. Foley, Local structure of nanoporous carbons, Phil. Mag. B 79 (10) (1999) 1519–1530.
[41] D.-Y. Kim, Y. Nishiyama, M. Wada, S. Kuga, Graphitization of highly crystalline cellulose, Carbon 39 (7) (2001) 1051–1056.
[42] E. Frank, L.M. Steudle, D. Ingildeev, J.M. Spörl, M.R. Buchmeiser, Carbon fibers: precursor systems, processing, structure, and properties, Angew. Chem. Int. Ed. 53 (21) (2014) 5262–5298.
[43] J. Scheirs, G. Camino, W. Tumiatti, Overview of water evolution during the thermal degradation of cellulose, Eur. Polym. J. 37 (5) (2001) 933–942.
[44] V. Mamleev, S. Bourbigot, M. Le Bras, J. Yvon, The facts and hypotheses relating to the phenomenological model of cellulose pyrolysis: interdependence of the steps, J. Anal. Appl. Pyrol. 84 (1) (2009) 1–17.
[45] Y. Qiao, S. Chen, Y. Liu, H. Sun, S. Jia, J. Shi, et al., Pyrolysis of chitin biomass: TG–MS analysis and solid char residue characterization, Carbohydr. Polym. 133 (2015) 163–170.
[46] S. Julien, E. Chornet, P.K. Tiwari, R.P. Overend, Vacuum pyrolysis of cellulose: Fourier transform infrared characterization of solid residues, product distribution and correlations, J. Anal. Appl. Pyrol. 19 (1991) 81–104.
[47] A.I. Ferreiro, M. Rabaçal, M. Costa, P. Giudicianni, C.M. Grottola, R. Ragucci, Modeling the impact of the presence of KCl on the slow pyrolysis of cellulose, Fuel 215 (2018) 57–65.
[48] S. Julien, E. Chornet, R.P. Overend, Influence of acid pretreatment (H2SO4, HCl, HNO3) on reaction selectivity in the vacuum pyrolysis of cellulose, J. Anal. Appl. Pyrol. 27 (1) (1993) 25–43.
[49] Y. Long, Y. Yu, Y.W. Chua, H. Wu, Acid-catalysed cellulose pyrolysis at low temperatures, Fuel 193 (2017) 460–466.
[50] F.J. Kilzer, A. Broido, Speculations on the nature of cellulose pyrolysis, Pyrodynamics 2 (151–163) (1965) 151–163, 2.
[51] W. Chaiwat, I. Hasegawa, T. Tani, K. Sunagawa, K. Mae, Analysis of cross-linking behavior during pyrolysis of cellulose for elucidating reaction pathway, Energy Fuel. 23 (12) (2009) 5765–5772.
[52] B. Hu, Q. Lu, Y.-t. Wu, Z.-x. Zhang, M.-s. Cui, D.-j. Liu, et al., Catalytic mechanism of sulfuric acid in cellulose pyrolysis: a combined experimental and computational investigation, J. Anal. Appl. Pyrol. 134 (2018) 183–194.
[53] D. Deldicque, J.-N. Rouzaud, B. Velde, A Raman–HRTEM study of the carbonization of wood: a new Raman-based paleothermometer dedicated to archaeometry, Carbon 102 (2016) 319–329.
[54] F. Tuinstra, J.L. Koenig, Raman spectrum of graphite, J. Chem. Phys. 53 (3) (1970) 1126–1130.
[55] J. McDonald-Wharry, M. Manley-Harris, K. Pickering, Carbonisation of biomass-derived chars and the thermal reduction of a graphene oxide sample studied using Raman spectroscopy, Carbon 59 (2013) 383–405.
[56] J.S. McDonald-Wharry, M. Manley-Harris, K.L. Pickering, Reviewing, combining, and updating the models for the nanostructure of non-graphitizing carbons produced from oxygen-containing precursors, Energy Fuel. 30 (10) (2016) 7811–7826.
[57] S. Yamauchi, Y. Kurimoto, Raman spectroscopic study on pyrolyzed wood and bark of Japanese cedar: temperature dependence of Raman parameters, J. Wood Sci. 49 (3) (2003) 235–240.
[58] K. Ishimaru, T. Hata, P. Bronsveld, D. Meier, Y. Imamura, Spectroscopic analysis of carbonization behavior of wood, cellulose and lignin, J. Mater. Sci. 42 (1) (2007) 122–129.
[59] A.E. Lewandowska, C. Soutis, L. Savage, S.J. Eichhorn, Carbon fibres with ordered graphitic-like aggregate structures from a regenerated cellulose fibre precursor, Compos. Sci. Technol. 116 (2015) 50–57.
[60] K. Kong, L. Deng, I.A. Kinloch, R.J. Young, S.J. Eichhorn, Production of carbon fibres from a pyrolysed and graphitised liquid crystalline cellulose fibre precursor, J. Mater. Sci. 47 (14) (2012) 5402–5410.
[61] L. Deng, R.J. Young, I.A. Kinloch, Y. Zhu, S.J. Eichhorn, Carbon nanofibres produced from electrospun cellulose nanofibres, Carbon 58 (2013) 66–75.
[62] I. Dallmeyer, L.T. Lin, Y. Li, F. Ko, J.F. Kadla, Preparation and characterization of interconnected, kraft lignin-B ased carbon fibrous materials by electrospinning, Macromol. Mater. Eng. 299 (5) (2014) 540–551.
[63] A. Cuesta, P. Dhamelincourt, J. Laureyns, A. Martinez-Alonso, J.M. Tascon, Comparative performance of X-ray diffraction and Raman microprobe techniques for the study of carbon materials, J. Mater. Chem. 8 (12) (1998) 2875–2879.
[64] P. Ouzilleau, A.E. Gheribi, P. Chartrand, G. Soucy, M. Monthioux, Why some carbons may or may not graphitize? The point of view of thermodynamics, Carbon 149 (2019) 419–435.
[65] J.-M. Vallerot, X. Bourrat, A. Mouchon, G. Chollon, Quantitative structural and textural assessment of laminar pyrocarbons through Raman spectroscopy, electron diffraction and few other techniques, Carbon 44 (9) (2006) 1833–1844.
[66] A.C. Ferrari, S.E. Rodil, J. Robertson, Interpretation of infrared and Raman spectra of amorphous carbon nitrides, Phys. Rev. B 67 (15) (2003), 155306-1 - 155306-20.
[67] A.C. Ferrari, J. Robertson, Raman spectroscopy of amorphous, nanostructured, diamond–like carbon, and nanodiamond, Philos. Trans. R. Soc. London, Ser. A: Mathematical, Physical and Engineering Sciences 362 (1824) (2004) 2477–2512.
[68] S. Prawer, F. Ninio, I. Blanchonette, Raman spectroscopic investigation of ion-beam-irradiated glassy carbon, J. Appl. Phys. 68 (5) (1990) 2361–2366.
[69] A. Nieto-Márquez, I. Espartero, J.C. Lazo, A. Romero, J.L. Valverde, Direct synthesis of carbon and nitrogen–carbon nanospheres from aromatic hydrocarbons, Chem. Eng. J. 153 (1–3) (2009) 211–216.
[70] J. Mandumpal, S. Gemming, G. Seifert, Curvature effects of nitrogen on graphitic sheets: structures and energetics, Chem. Phys. Lett. 447 (1–3) (2007) 115–120.
[71] S. Stafström, Reactivity of curved and planar carbon–nitride structures, Appl. Phys. Lett. 77 (24) (2000) 3941–3943.
[72] S. Rajabpour, Q. Mao, Z. Gao, M.K. Talkhoncheh, J. Zhu, Y. Schwab, et al., Low-temperature carbonization of polyacrylonitrile/graphene carbon fibers: a combined ReaxFF molecular dynamics and experimental study, Carbon 174 (2021) 345–356.
[73] C. Gómez-Navarro, J.C. Meyer, R.S. Sundaram, A. Chuvilin, S. Kurasch, M. Burghard, et al., Atomic structure of reduced graphene oxide, Nano Lett. 10 (4) (2010) 1144–1148.
[74] S. Gupta, A. Saxena, Nanocarbon materials: probing the curvature and topology effects using phonon spectra, J. Raman Spectrosc.: An International Journal for Original Work in all Aspects of Raman Spectroscopy, Including Higher Order Processes, and also Brillouin and Rayleigh Scattering 40 (9) (2009) 1127–1137.
[75] H. Sjöström, S. Stafström, M. Boman, J.E. Sundgren, Superhard and elastic carbon nitride thin films having fullerenelike microstructure, Phys. Rev. Lett. 75 (7) (1995) 1336–1339.
[76] J.D. Kim, J.-S. Roh, M.-S. Kim, Effect of carbonization temperature on crystalline structure and properties of isotropic pitch-based carbon fiber, Carbon letters 21 (2017) 51–60.
[77] S.-X. Zhao, N. Ta, X.-D. Wang, Effect of temperature on the structural and physicochemical properties of biochar with apple tree branches as feedstock material, Energies 10 (9) (2017), 1293-1 - 1293-15.
[78] A.J.R. de Castro, G.D. Saraiva, A.C. Oliveira, V.O.S. Neto, A.J. Paula, A.G. Souza Filho, et al., Ordered porous carbons from hydrothermally treated biomass: effects of the thermal treatments on the structure and porosity, Vib. Spectrosc. 111 (2020), 103175-1 - 103175-11.
[79] S.E. Rodil, Bonding structure in carbon nitride films, *Recent Res. Devel.* Applied Phys 6 (2003) 391–426.
[80] R. Gago, I. Jiménez, J. Neidhardt, B. Abendroth, I. Caretti, L. Hultman, et al., Correlation between bonding structure and microstructure in fullerenelike carbon nitride thin films, Phys. Rev. B 71 (12) (2005), 125414-1 - 125414-6.
[81] R. Gago, J. Neidhardt, M. Vinnichenko, U. Kreissig, Z. Czigány, A. Kolitsch, et al., Synthesis of carbon nitride thin films by low-energy ion beam assisted evaporation: on the mechanisms for fullerene-like microstructure formation, Thin Solid Films 483 (1–2) (2005) 89–94.
[82] L. Hultman, J. Neidhardt, N. Hellgren, H. Sjöström, J.-E. Sundgren, Fullerene-like carbon nitride: a resilient coating material, MRS Bull. 28 (3) (2003) 194–202.
[83] I. Jiménez, R. Gago, J.M. Albella, L.J. Terminello, X-ray absorption studies of bonding environments in graphitic carbon nitride, Diam. Relat. Mater. 10 (3–7) (2001) 1170–1174.
[84] N. Hellgren, M.P. Johansson, E. Broitman, L. Hultman, J.-E. Sundgren, Role of nitrogen in the formation of hard and elastic CN x thin films by reactive magnetron sputtering, Phys. Rev. B 59 (7) (1999) 5162–5169.
[85] S.R. Kelemen, M. Afeworki, M.L. Gorbaty, P.J. Kwiatek, M.S. Solum, J.Z. Hu, et al., XPS and 15N NMR study of nitrogen forms in carbonaceous solids, Energy Fuel. 16 (6) (2002) 1507–1515.
[86] G. Lawrie, I. Keen, B. Drew, A. Chandler-Temple, L. Rintoul, P. Fredericks, et al., Interactions between alginate and chitosan biopolymers characterized using FTIR and XPS, Biomacromolecules 8 (8) (2007) 2533–2541.
[87] X. Fan, L. Zhang, G. Zhang, Z. Shu, J. Shi, Chitosan derived nitrogen-doped microporous carbons for high performance CO2 capture, Carbon 61 (2013) 423–430.
[88] W.J. Gammon, O. Kraft, A.C. Reilly, B.C. Holloway, Experimental comparison of N (1s) X-ray photoelectron spectroscopy binding energies of hard and elastic amorphous carbon nitride films with reference organic compounds, Carbon 41 (10) (2003) 1917–1923.
[89] Q. Liu, Z. Chen, S. Jing, H. Zhuo, Y. Hu, J. Liu, et al., A foldable composite electrode with excellent electrochemical performance using microfibrillated cellulose fibers as a framework, J. Mater. Chem. 6 (41) (2018) 20338–20346.
[90] Y. Zhang, L. Lu, S. Zhang, Z. Lv, D. Yang, J. Liu, et al., Biomass chitosan derived cobalt/nitrogen doped carbon nanotubes for the electrocatalytic oxygen reduction reaction, J. Mater. Chem. 6 (14) (2018) 5740–5745.
[91] A.G. Kudashov, A.V. Okotrub, L.G. Bulusheva, I.P. Asanov, Y.V. Shubin, N.F. Yudanov, et al., Influence of Ni– Co catalyst composition on nitrogen content in carbon nanotubes, J. Phys. Chem. B 108 (26) (2004) 9048–9053.
[92] Z. Xing, Z. Ju, Y. Zhao, J. Wan, Y. Zhu, Y. Qiang, et al., One-pot hydrothermal synthesis of Nitrogen-doped graphene as high-performance anode materials for lithium ion batteries, Sci. Rep. 6 (1) (2016) 1–10.
[93] P. Lespade, A. Marchand, M. Couzi, F. Cruege, Caracterisation de materiaux carbones par microspectrometrie Raman, Carbon 22 (4–5) (1984) 375–385.
[94] M.-A. Kim, D. Jang, S. Tejima, R. Cruz-Silva, H.-I. Joh, H.C. Kim, et al.,

Strengthened PAN-based carbon fibers obtained by slow heating rate carbonization, Sci. Rep. 6 (2016), 22988-1 - 22988-7.
[95] J. Neidhardt, Z. Czigány, I.F. Brunell, L. Hultman, Growth of fullerene-like carbon nitride thin solid films by reactive magnetron sputtering; role of low-energy ion irradiation in determining microstructure and mechanical properties, J. Appl. Phys. 93 (5) (2003) 3002–3015.
[96] A. Deurbergue, A. Oberlin, Stabilization and carbonization of pan-based carbon fibers as related to mechanical properties, Carbon 29 (4–5) (1991) 621–628.
[97] Z. Czigány, I.F. Brunell, J. Neidhardt, L. Hultman, K. Suenaga, Growth of fullerene-like carbon nitride thin solid films consisting of cross-linked nano-onions, Appl. Phys. Lett. 79 (16) (2001) 2639–2641.
[98] S.M. Aldosari, M. Khan, S. Rahatekar, Manufacturing carbon fibres from pitch and polyethylene blend precursors: a review, Journal of Materials Research and Technology 9 (4) (2020) 7786–7806.
[99] H. Xiao, Y. Lu, M. Wang, X. Qin, W. Zhao, J. Luan, Effect of gamma-irradiation on the mechanical properties of polyacrylonitrile-based carbon fiber, Carbon 52 (2013) 427–439.
[100] W. Watt, Production and properties of high modulus carbon fibres, Proceedings of the Royal Society of London. A. Mathematical and Physical Sciences 319 (1536) (1970) 5–15.